Plant Science 265 (2017) 100–111

Contents lists available at ScienceDirect

Plant Science

journal homepage: www.elsevier.com/locate/plantsci

The NOS-like protein from the microalgae *Ostreococcus tauri* is a genuine and ultrafast NO-producing enzyme

Marine Weisslocker-Schaetzel[a], François André[a], Nabila Touazi[a], Noelia Foresi[b], Mehdi Lembrouk[a], Pierre Dorlet[a], Annie Frelet-Barrand[a], Lorenzo Lamattina[b], Jérôme Santolini[a,*]

[a] *Institute for Integrative Biology of the Cell (I2BC), CEA, CNRS, Univ Paris-Sud, Université Paris-Saclay, F-91198, Gif-sur-Yvette cedex, France*
[b] *Instituto de Investigaciones Biologicas, Facultad de Ciencias Exactas y Naturales, Universidad Nacional de Mar del Plata, CC 1245, 7600 Mar del Plata, Argentina, Argentina*

ARTICLE INFO

Keywords:
NO synthase
Plant
Algae
Catalysis
Function
Structure

ABSTRACT

The exponential increase of genomes' sequencing has revealed the presence of NO-Synthases (NOS) throughout the tree of life, uncovering an extraordinary diversity of genetic structure and biological functions. Although NO has been shown to be a crucial mediator in plant physiology, NOS sequences seem present solely in green algae genomes, with a first identification in the picoplankton species *Ostreococcus tauri*. There is no rationale so far to account for the presence of NOS in this early-diverging branch of the green lineage and its absence in land plants. To address the biological function of algae NOS, we cloned, expressed and characterized the NOS oxygenase domain from *Ostreococcus tauri* (OtNOSoxy). We launched a phylogenetic and structural analysis of algae NOS, and achieved a 3D model of OtNOSoxy by homology modeling. We used a combination of various *spectroscopies* to characterize the structural and electronic fingerprints of some OtNOSoxy reaction intermediates. The analysis of OtNOSoxy catalytic activity and kinetic efficiency was achieved by stoichiometric stopped-flow. Our results highlight the conserved and particular features of OtNOSoxy structure that might explain its ultrafast NO-producing capacity. This integrative Structure-Catalysis-Function approach could be extended to the whole NOS superfamily and used for predicting potential biological activity for any new NOS.

1. Introduction

Nitrogen monoxide (NO) is an extremely reactive radical molecule that has long been considered as a toxic, polluting and harmful gas [1]. A few decades ago, the biological history of NO unfolded thanks to the discovery of its central role in the regulation of mammalian vascular tone. The biological source of NO was identified soon after as being three different isoforms of a family of enzymes, named NO-Synthases (NOS). Despite significant differences (histological and subcellular localization, expression profiles, catalytic regulation [2–4]) these isoforms were found to share the same quaternary organization, the same crystallographic structure of their catalytic site and the same catalytic mechanism. If NO has become a ubiquitous signaling molecule regulating many physiological processes such as neural communication, cell cycle, metabolism [5], a considerable part of NOS/NO biochemical history remains related to the cytotoxic reactivity of NO and the utilization of NO and Reactive Nitrogen Species (RNS) in the non-specific immune response [6]. Today, because of the complexity of NO biological chemistry, it is becoming more and more difficult to account for the multiple functions of NOS and NO (from signaling to oxidative stress) and to understand the paradox of NOSs that are at the same time the support of essential physiological functions and the source of numerous pathological conditions [7].

The presence of hundreds of NOS throughout the Tree of Life (personal data) has added another layer of complexity. Indeed, NOSs have been found in all kingdoms of life, in archaea, bacteria, fungi, insects, crustacean, fishes… [8–12]. As the predominant paradigm of the NO field is mostly based on the relation "NOS → NO → Signaling", the newly discovered NOS were *a priori* assigned the same catalytic functioning and the same biological function, namely producing NO

Abbreviations: Arg, L-arginine; BH_4, tetrahydrobiopterin, (6R)-5,6,7,8-tetrahydro-L-biopterin; CO, carbon monoxide; NO, nitric oxide; NOHA, N^{ω}-hydroxy-L-arginine; NOS, nitric oxide synthase; bacNOS, bacterial nitric oxide synthase; bsNOS, nitric oxide synthase from *Bacillus subtilis*; eNOS, bovine endothelial nitric oxide synthase; iNOS, murine inducible nitric oxide synthase; mNOS, mammalian nitric oxide synthase; nNOS, rat neuronal nitric oxide synthase; OtNOS, nitric oxide synthase from *Ostreococcus tauri*; NOSoxy, oxygenase domain of NOS; RNS, Reactive Nitrogen Species; ROS, Reactive Oxygen Species

* Corresponding author at: Laboratoire Stress Oxydant et Détoxication, Institute for Integrative Biology of the Cell (I2BC), CEA, CNRS, Univ Paris-Sud, Université Paris-Saclay, F-91198, Gif-sur-Yvette cedex, France.
E-mail address: jerome.santolini@cea.fr (J. Santolini).

http://dx.doi.org/10.1016/j.plantsci.2017.09.019
Received 27 April 2017; Received in revised form 21 September 2017; Accepted 24 September 2017
Available online 28 September 2017
0168-9452/

and mediating signals [5]. Though, these NOSs have been poorly characterized in comparison with their mammalian counterparts and only a few NOSs from drosophila [13,14], amoeba [10,15] and bacteria [16–24] have been investigated.

Since the late 90s, NO has emerged as a major signaling molecule in plants [25], involved in processes as diverse as plant immunity [26], systemic acquired resistance [27], growth and development [28], N_2-fixing symbiosis tuning [29], or abiotic stresses response [30]. If NO was shown to interact with other signaling molecules, including ROS, Ca^{2+} and hormones such as auxin, salicylic acid and abscisic acid, the precise ways of its biological activity remain to be established [26]. The source of NO production has been and remains also a matter of debate in plants [31,32]. Because of the central role of NO, the discovery of a NOS-like protein in *Arabidopsis thaliana* was proposed [33–35] but rapidly questioned. Indeed, the analysis of the genome of *A. thaliana* and later of those of other higher plants led to the surprising conclusion that there were no mammalian-like NOSs in plants. Today the actual source of NO, the nature of the substrate (Arg, nitrite, nitrate, polyamines) and of the triggered signal (Ca^{2+}, ROS, cGMP) still remains to be determined [36–40].

In this very context, the laboratory of Lamattina (Mar del Plata University, Argentina) spotted in 2010 the presence of a NOS-related sequence [9] in the genome of the microalgae *Ostreococcus tauri* [41]. Ostreococcus belongs to the class of the mammielophyceae,[1] an early-diverging branch (at least 700 million years ago) from the green plant lineage. This picophytoplankton is the smallest eukaryote found to date. It bears a small and compacted genome, with only one mitochondria and one chloroplast. Its broad diffusion corresponds to various ecological niches from coastal to oligotrophic waters, from deep-see to high-irradiance exposure. NOSs have been also detected in other species from this taxon including *Ostreococcus lucimarinus* and *Bathycoccus prasinos* [8]. More recently, using the 1000 Plants (1KP) international multidisciplinary consortium's transcriptome database (www.onekp.com), Wendehenne and colleagues showed that NOSs were to be found in some other species throughout the various classes of algae [42]. NOSs sequence was even found in the fresh-water algae *Chaetosphaeridium globosum*, a member of the Coleochaetophyceae class, a class that is the closest branch to terrestrial plants. However, no NOS sequence has been found in land plants so far, which could be rationalized by at least two hypotheses: (i) NOS sequences were lost during the evolution or (ii) they never have been present. In the first hypothesis, a large range of algae and especially some that have experienced a strong compaction genome would have conserved this enzyme throughout evolution. In the second hypothesis *O. tauri* and the other algae would have gained – from horizontal genome transfer – and conserved the NOS sequences during their evolution as an independent event, perhaps even after land colonization by terrestrial plants. In both cases this questions the reason of the presence of such an enzyme in *O. tauri* and these various algae. Is there any ecological specificity to this organism that required NOS and its beneficial activity? Which biochemical activity NOS is supposed to play in these organisms, and is it related to the catalytic production of NO like in animals?

The characterization of NOS biological activity from these algae is the first necessary step to deal with these questions, with *Ostreococcus* as the best-suited model. The first functional characterization confirmed that NO production in *O. tauri* was OtNOS- and L-Arg dependent and was shown to increase under high light irradiance, suggesting a role of OtNOS in the repair or the defense against photo-induced oxidative damage [9]. More recently, Foresi and colleagues transformed *A. thaliana* plants with OtNOS and observed an increased NO production in relation with a greater resistance to water stress [43]. At this stage, deciphering OtNOS biochemistry constitutes an excellent opportunity to go further into NOS biological chemistry. In this regard, we present here our results on OtNOS structural and functional characterization. Using a combination of spectroscopies and fast kinetics, we comparatively analyzed OtNOS catalytic and kinetic efficiency, its interaction with ligand, substrate and cofactor, and its capacity to produce NO. OtNOS appears as genuine NOS, with similar spectroscopic fingerprints to mammalian NOSs and high NO producing capacity.

2. Experimental procedures

2.1. Bioinformatics and computational

All NOS protein sequences were extracted from NCBI by similarity search from either OtNOS or *Mus musculus* iNOS sequences. For phylogenetic analysis, 39 full-length sequences of NOSs representative of the genetic diversity of this family of proteins were selected (see Fig. 1 legend). Phylogenetic trees were computed through Seaview 4.5 graphical interface using PhyML algorithm, and the figures produced by FigTree.

Jalview 2.8 software was used to generate various multiple sequence alignments. Different algorithms were applied (ClustalW, Muscle, Probcons) and compared. By assessment with the three-dimensional structures of mammal and bacterial NOSs available in PDB, the PROBCONS alignment was considered and further used for phylogeny and homology modeling procedures.

For homology modeling procedure, the set of NOS sequences used for phylogenetic analysis was restrained to a subset of 16 sequences including the 3 algae species, 3 cyanobacteria, 3 mammalian, 3 bacterial, 1 fungal, 1 insect, 1 mollusk, and 1 diatom sequences. This subset was set up for anchoring precisely the NOS oxygenase domains that appeared to be well-conserved in the multiple alignments. The oxygenase domain sequences of algae NOSs were then extracted from the PROBCONS multiple alignment based on the overlap with the well-characterized iNOSoxy domain (segment 127-494 in *Mus musculus* iNOS residue numbering). Among the 16 species of the subset, 5 have been crystallized and structurally determined. This allowed refining the PROBCONS alignment by manual adjustment (see Fig. 2 and S1 in Supplementary material).

The three-dimensional model of *Ostreococcus tauri* NO-synthase oxygenase domain was rebuilt using the homology modeling suite Modeller (9v14) with 1NOD PDB structure as template (chain A). The Cys49-Lys434 domain of OtNOS was rebuilt from the alignment with the segment Cys109-Gln496 of 1NOD chain A structure. The cofactors HEM and BH4, and the substrate ARG have been included in the pairwise alignment, for rebuilding an OtNOS model in the catalytical state. The validated pairwise sequence alignment used as input for Modeller is the same as that displayed in Fig. 2 and S1 in Supplementary material, by extracting lines 4 (*Mus*) and 5 (*Ostreococcus*) from the multiple alignment. Runs of 100 models were performed with a further loop refinement protocol, and the generated models sorted by the MODELLER objective function were evaluated by their DOPE (Discrete Optimized Protein Energy) and GA341 scores calculated by Modeller. The best models corresponding to the lowest DOPE score and best objective function issued from each run were pooled and submitted to the online metaserver SAVES (Structural Analysis and Verification Server: http://services.mbi.ucla.edu/SAVES), and finally to the QMEAN scoring function server (https://swissmodel.expasy.org/qmean) for model quality assessment. The final model was the best one according to a good compromise between the scores calculated by the SAVES server scoring programs and the QMEAN value. As a result, the selected OtNOS structural model had a DOPE score of −41721 and QMEAN score equal to 0.690, which is good when compared to the QMEAN scores of individual iNOS PDB templates. Other mono-template 3D models were rebuilt with various mammal and bacterial structures available in PDB, and the 1NOD template gave the best DOPE and QMEAN scores.

[1] http://www.algaebase.org/search/species/detail/?species_id = T6f1f7ac43489a845.

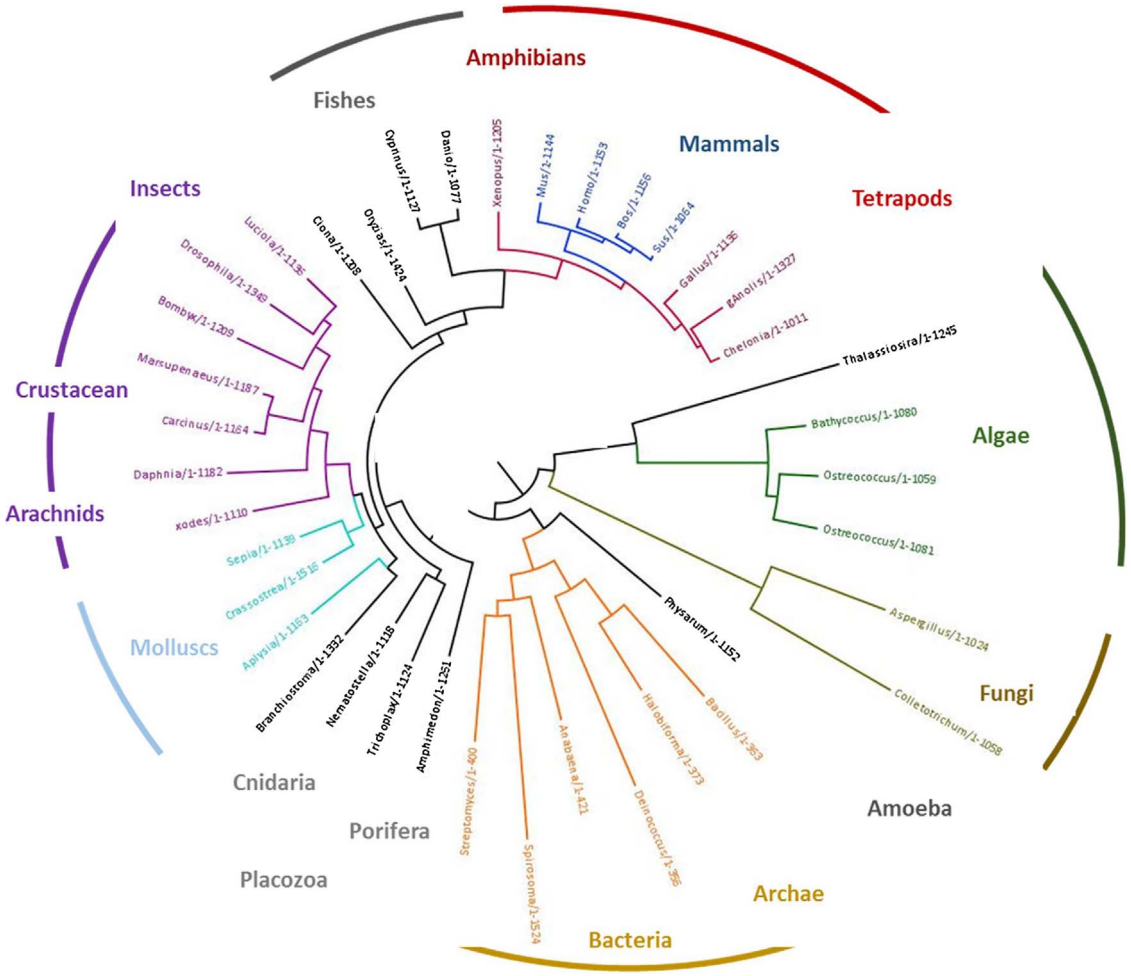

Fig. 1. Maximum likelihood phylogenetic tree of microalgae NOSs aligned with a series of NOSs representative of the bacteria, cyanobacteria and mammal phyla.
The set of sequences includes the 3 microalgae NOSs (green), and a selection of species representative of the phylogenetic diversity of NOS genes: 4 mammalian NOSs (dark blue), 4 NOSs from other tetrapodes (red), 6 bacterial NOSs (orange), 2 NOSs from fungi (brown), 3 NOSs from mollusks (light blue), 7 NOSs from arthropods (magenta), and various NOSs from diatoms, amoeba, cnidaria, placozoa, porifera, arachnids, cephalocordata, tunicata. Probcons algorithm provided by Jalview 2.8 interface was applied to generate multiple sequence alignments. The phylogenetic tree was generated via Seaview software (version 4.5.4) [88] using PhyML algorithm, with LG model as substitution model, approximate Likelihood-ratio test for branches (aLRT, SH-like), and NNI tree topology improvement using BioNJ distance-based tree as starting tree.

2.2. Cloning and expression of OtNOSoxy

Molecular cloning of *Ostreococcus tauri* NO-Synthases. The *Ostreococcus tauri* full-length NOS (OtNOS) coding DNA sequence was synthesized, sequenced, and cloned into pUC57 using *Xba*I and *Xho*I enzymes [9]. The cDNA fragment corresponding to the oxygenase domain (1-437 AA) has been amplified by PCR in order to subclone the *Nde*I-*BamH*I fragment into pET15b vector. All PCR fragments and plasmids were verified by sequencing. All cloning steps were performed into *E. coli* strains DH5α. After sequencing, constructions were used to transform Rosetta (DE3) *E. coli* strains, more suitable for high protein expression [44].

Expression and purification of the oxygenase domain of OtNOS (OtNOSoxy). OtNOSoxy was overexpressed and purified as previously described [45,46]. OtNOSoxy was expressed in *E. coli* cultures of terrific broth containing 125 mg/L ampicillin. Protein expression was induced by adding 1 mM isopropyl-β-D thiogalactoside, and the cultures were supplemented with 500 µM −aminolevulinic acid. After 72 h of growth at 20 °C, the cells were harvested by centrifugation at 6000 rpm for 20 min at 4 °C. After one cycle of freeze (−80 °C)-thaw, bacteria were resuspended in ice-cold lysis buffer (0.04 M Tris-HCl, pH7.4, 10% glycerol, 0.25 M NaCl) containing 1 mg/mL lysozyme, 0.5 µg/mL each leupeptin and pepstatin, 1 mM phenylmethanesulfonyl fluoride (PMSF), Pefabloc (0,120 µg/L) and 50 U/mL DNase I (bovine pancreas type IV, Sigma) with or without 10 µM BH_4 in ascorbic acid and 10 mM L-arginine.

Cells were lysed using continuous-flow Cell disruption equipment (Constant Systems Ltd, United Kingdom). The lysate was centrifuged at 16,000 rpm for 45 min at 4 °C. The supernatant was mixed with Ni-Nta resin (Novagen) equilibrated with MCAC buffer (0.04 M Tris-HCl, pH7.4, 10% glycerol, 0.15 M NaCl, 1 mM PMSF) in the presence or absence of 10 µM BH_4 and 10 mM L-arginine. Resin was stacked into a column and washed with 5 vol of MCAC buffer and 5 vols of MCAC Buffer supplemented with 60 mM imidazole. Bound protein was eluted with MCAC buffer containing 300 mM imidazole. Column fractions were pooled and concentrated using Centriprep (Millipore, Bedford, MA).

2.3. Samples preparation

Samples were reconditioned in a 100 mM KPi buffer, pH 7.4, 10% glycerol, 150 mM NaCl in the presence of different combinations of Arg (5 or 10 mM) and/or BH_4 (100 µM to 1 mM in 3 mM DTT) by three successive cycles of dilution/centrifugation in the final buffer using MicroCon membrane concentrators with a 30 kDa cut-off (Millipore). Anaerobic ferric NOS (Fe^{III}) was first prepared by 100 cycles of alternate vacuum and argon refilling over 20 min, directly in a quartz EPR tube (EPR experiments) or in a quartz cuvette (UV–vis spectrometry),

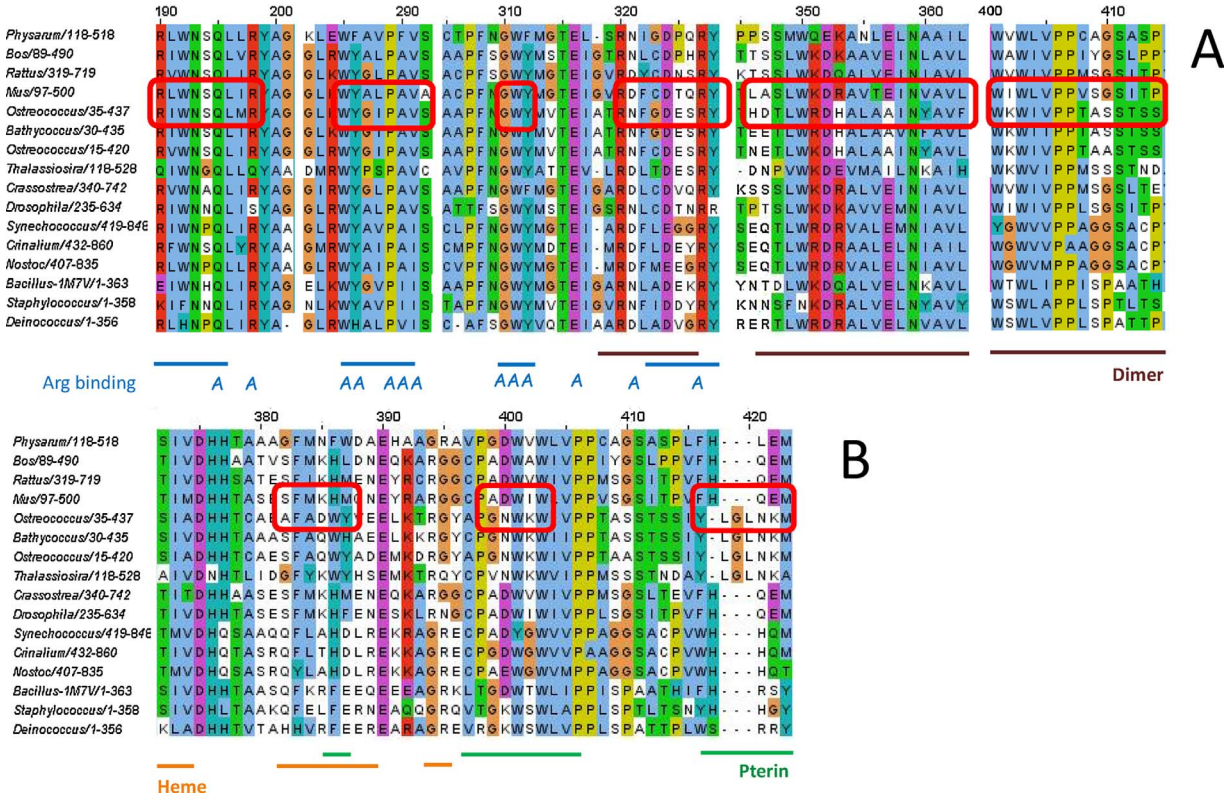

Fig. 2. Multiple sequence alignment of essential regions from three microalgae NOSoxy domains and a series of NOSoxy representative of the bacteria, cyanobacteria and mammals phyla used for the phylogenetic analysis.

Multiple sequence alignments showing essential regions from the oxygenase domain of NO-Synthases (NOSoxy). The sequences aligned are (GI numbers in parenthesis): *Physarum polycephalum* (126573158) endothelial NOS from *Bos Taurus* (317008623) and neuronal NOS from *Rattus norvegicus* (1527149), inducible NOS from *Mus musculus* (6754872), NOS from *Ostreococcus tauri* (308812915), *Bathycoccus prasinos* (612390834), *Ostreococcus lucimarinus* (144582176), *Thalassiosira oceanica* (397591314), *Crassostrea gigas* (762163733), *Drosophila melanogaster* (7297764), *Synechococcus sp*. PCC7335 (196188428), *Crinalium epipsammum* (428248029), *Nostoc sp*. PCC 7107 (427361656), *Bacillus subtilis* (349597920), *Staphylococcus aureus* (323439859), *Deinococcus radiodurans* (499191681). ClustalX color code as follows: blue for hydrophobic (ILMAV) and aromatic (FW) residues, violet for positively charged polar residues (ED), red for negatively charged polar residues (RK), light green for non-polar residues (QST), orange for glycine, green for polar aromatic residues (HT), yellow for proline, and pink for cysteine. Jalview © software (v2.8) was used as graphical interface and PROBCONS © as protein multiple sequence alignment program. See Fig. S1 in Supplementary material for the complete alignment and the methodological details. Regions of interest for iNOs and otNOS sequences are highlighted in red boxes. Panel A. Regions with residues involved in Arg binding (blue dash and A letters) and dimer interface (brown dash). Panel B. C-terminal domain showing residues involved in heme binding (orange dash) and pterin binding (green dash).

both sealed with air-tight rubber septa. Ferrous samples (Fe^{II}) were obtained by reduction of Fe^{III} NOS with the addition of a small volume of dithionite solution (5–100 mM). Ferrous heme-CO ($Fe^{II}CO$) and heme-NO samples were then obtained by flushing CO/NO gas directly inside the EPR tube (or the cuvette) for 10 min to ensure CO/NO saturation of the solution and complete CO/NO binding. All UV–vis spectra were recorded at room temperature on an Uvikon XL spectrophotometer (Serlabo, Entraigues sur la Sorgue, France).

2.4. EPR characterization

9.4 GHz EPR (X-band) spectra were recorded on a Bruker Elexsys 500 spectrometer equipped either with a standard (9.49 GHz) or a high-resolution (9.38 GHz) TE cavity (Bruker), a continuous-flow ESR 900 cryostat and an ITC504 temperature controller (Oxford Instruments, Abingdon, UK). Simulations were performed with the Easyspin software package[47] and routines written in the lab. The EPR parameters that were used for the simulations are reported in the corresponding tables.

2.5. Stoichiometric stopped-flow

OtNOSoxy (30–40 μM) were conditioned in a buffer (0.1 M KPi pH 7.4, 10% glycerol), containing the substrate (Arg 5 mM or NOHA 500 μM) and cofactor (BH_4 500 μM), by 3–5 dilution/concentrating cycles. Anaerobic Fe^{III} NOS was then obtained by 100 cycles of alternate vacuum and argon refilling, directly into a quartz cuvette. This sample was diluted with anaerobic conditioning buffer, using a gas-tight syringe, to a final NOS concentration of about 20–25 μM. Fe^{III} NOS was reduced to Fe^{II} NOS using a freshly prepared anaerobic solution of 32 mM sodium dithionite. The reduction was followed by UV–vis spectroscopy to ensure the complete reduction of the protein and avoid dithionite excess.

The rapid-mixing stopped-flow experiments were performed at 4 °C on a Bio-Logic SFM 300 instrument customized for anaerobic and semianaerobic experiments and connected to a Tidas 1024-diode array detector able of recording spectra every 3 ms. One SFM syringe was first washed with dithionite to scavenge any residual oxygen and then with anaerobic buffer (0.1 M KPi pH 7.4, 10% glycerol) to remove excess dithionite. The Fe^{II} NOS samples were transferred to the SFM anaerobic syringe and rapidly mixed with air-saturated buffer (0.1 M KPi pH 7.4), in a 1:1 ratio, at 4 °C. The reaction was monitored using a diode array detector that allows the recording of one spectrum every 3 ms. Kinetic analyses were achieved using the SFit routine (Bio-logic) and by directly simulating the kinetic traces to multi-exponential functions (Origin 8.0 ©).

3. Results

3.1. Phylogenetic tree of NOS including algae NOSs

We first achieved a phylogenetic analysis of 40 proteins from the NOS family that included three microalgae NOSs (namely *Ostreococcus tauri, Ostreococcus lucimarinus* and *Bathycoccus prasinos*), the four studied mammalian NOSs and various NOSs from archaea, bacteria, cnidarian, porifera, molluscs, arthropods, insects, fishes, amphibians and reptiles (Fig. 1). The distribution of metazoan NOS matches the standard evolution tree of this Phylum. However, algae NOSs seem to follow a singular evolution path, disconnected from that of metazoan but also from that of bacteria. The origin of NOS in algae might neither be related to NOS in cyanobacteria nor to NOS from metazoan. In this regard, the closest NOS to algae NOSs is the one from the marine, planktonic diatom *Thalassiosira oceanica*, another photosynthetic organism.

3.2. Comparative alignment of OtNOS oxygenase sequence with bacterial and mammalian NOSs

We then performed a sequence alignment using the sequences of the three algae NOSs against a selection of NOSs representative of the phylogenetic diversity of NOS family (Fig. 2). We chose the three mammalian canonical NOS (nNOS from *Rattus norvegicus*, iNOS from *Mus musculus* and eNOS from *Bos bovis*), the three most studied bacterial NOSs (*Bacillus subtilis*, *Staphylococcus aureus*, *Deinococcus radiodurans*) and three cyanobacterial NOS that present a full-length NOS structure (*Synechococcus sp PCC7335*, *Crinalium epipsamum*, *Nostoc sp PCC 7107*). For comparison purpose, we added the NOSs from *Thalassiosira oceanica*, from the amoeba *Physarum polycephalum*, from a crustacean (*Crassostrea gigas*) and from an insect (*Drosophila melanogaster*).

Two types of alignments have been performed: either with full-length proteins or with only the oxygenase domains (with native bacterial NOSs and the truncated forms for the other NOSs). Both approaches led to the same results (not shown). As reported in previous articles [8,9], OtNOS displays most of the characteristic domains of a NO-Synthase: a reductase domain, an oxygenase domain, connected via a Ca-binding domain. When focusing on the oxygenase domain (Fig. S1 in Supplementary material), that harbors the NOS catalytic site, we globally observe a weak homology between OtNOS and NOSs from other clades (between 34.65 and 43.96% of identity). If the overall alignment shows a weak similarity, it appears concentrated in zones that are crucial for NOSs structural properties. This is illustrated by the conservation of residues that constitute the catalytic core of the oxygenase domain. Fig. 2 highlights the similarities and differences between the sequences of OtNOS and iNOS in the case of the global alignment. **Arg Binding.** Most of the residues involved in Arg binding or in the substrate access channel [48] are conserved (Fig. 2A), in particular E371/306 and W366/301 (that form H-bond with both Arg nitrogens) and Q257/189, Y367/302 (H-bond with the carboxylate terminal). The only modification we noticed is the conversion of D376 (iNOS) into N311 (OtNOS) that is also observed in eNOS, bsNOS and drosophila NOS and might not have significant structural impact. **Dimer interface.** Many parts of NOS sequence that contribute to its dimerization are missing (Fig. S1 in Supplementary material). The N-terminal hook that contains residues essential in monomer/dimer equilibrium [49,50] is completely absent from OtNOS sequence. So is the Zn/pterin binding domain. In particular the CxxxxC motif that is found in all eukaryotic NOSs (amoeba, insect and mollusks) is replaced by a CxxxC motif in OtNOS (Fig. S1 in Supplementary material) suggesting an impeded ability to build a Zn-tetrathiolate cluster. Likewise the C-Ter region of the oxygenase domain is much less conserved with an obvious insert in the helical lariat at the level of the β12a β-strand and the absence of the β12b β-strand. G464 is replaced by a S399, which unlike the Proline in bacterial NOS, might not provide additional hydrophobic contact and contribution to dimer interface. **Heme pocket.** We observe a strong identity of the hydrophobic residues that surround the heme (344-346 and 363-372 for iNOS, and 279-281, 298-307 for OtNOS). It is to be noted that OtNOS conserved a Valine residues at position 281, which is the landmark of the capacity of efficiently releasing NO [22,51–54]. The isoleucine observed at that position for bacterial NOSs slows down NO release by two orders of magnitude [22,52]. The other key-residues of the catalytic core are conserved, such as W188/119, F363/298 and the heme binding C194/125. Although the 448/449 residues (383/384 in OtNOS) are conserved, we observed strong variations in sequences in the C-terminal region in particular with a 3-residues insert in the helical lariat (483-485), which is believed to modify the exposed heme edge. **Pterin Binding.** As noticed here-above, The N-terminal hook that is involved in pterin binding [49,55] and the N-terminal pterin binding region are absent from OtNOS sequence, alike what is observed for bacterial NOSs [56]. Other major variations in residues involved in pterin binding are observed, such as H440 (W375), M441 (Y376) and I456 (K391) and again the region 470-474 (iNOS) that experiences a 3-residue insert. Also the major residues involved in BH_4 binding in iNOS are conserved (R375/310, W455/390, W457/392, [57] these changes suggest strong changes in the pterin cofactor binding.

Although OtNOS shares the same percentage of identity with mammalian and bacterial NOSs (37–38%) it seems to exhibit more of the required structural elements that are necessary to preserve NO producing ability. We investigated this structural similarity by generating a 3D model of the oxygenase domain of OtNOS by Homology Modelling.

3.3. Structural analysis of OtNOS oxygenase domain

This model was generated using Modeller9v12 with the crystallographic structure of iNOSoxy in the presence of Arg and BH_4 (PDB 1NOD) as template (see Experimental procedures [58,59]). The overall structure shows the same global architecture, a central winged β-structure surrounded by alpha-helices looking like a baseball catcher's mitt [60].

3.3.1. Arg

Fig. 3A displays the 3D of the heme pocket in OtNOS model. Connolly surface generated for residues surrounding Arg reveals a tight constrained, binding niche for Arg similar to the one observed for iNOSoxy [48] and bsNOS [56]. Indeed, as mentioned above, apart from the N376-D311 conversion, all residues involved in Arg binding most of the H-bonding and electrostatic interactions between Arg and its vicinal residues were conserved. The H-bond distances between Arg guanidinium moiety and the vicinal residues E306 and W301 were observed at 2.66 and 2.82 Å between the Glu306 carboxylate oxygen and the guanidinium Nω and Nε Nitrogens and 3.01 Å between the Trp366 carbonyl oxygen and the guanidinium Nε Nitrogen (2.72, 2.77 and 3.07 Å observed for iNOS 1NOD structure). Some differences were observed in the amino-acid side of Arg. Although the measured distances between Q189, Y276, Y302, E306 and Arg amine and carboxylate are similar, the N376-D311 conversion has moved the carbonyl moiety more than 3 Å away from Arg closest oxygen atom, suggesting some potential changes in Arg anchoring in the distal heme pocket.

3.3.2. Heme

The superimposition of the major residues in interaction with heme in iNOSoxy and OtNOS (Fig. 3B) suggests a strong similarity between the two heme pockets. Although some key-residues are modified (for example S236*vs*V167, R193*vs*K124 and Q199*vs*Y130), all OtNOS and iNOSoxy residues are superimposable (Fig. 3B). The residues forming the hydrophobic core of the heme pocket are strictly conserved, in particular V281 that tunes NO off-rate (Fig. 3B). This suggests a strongly conserved architecture of the heme distal and proximal

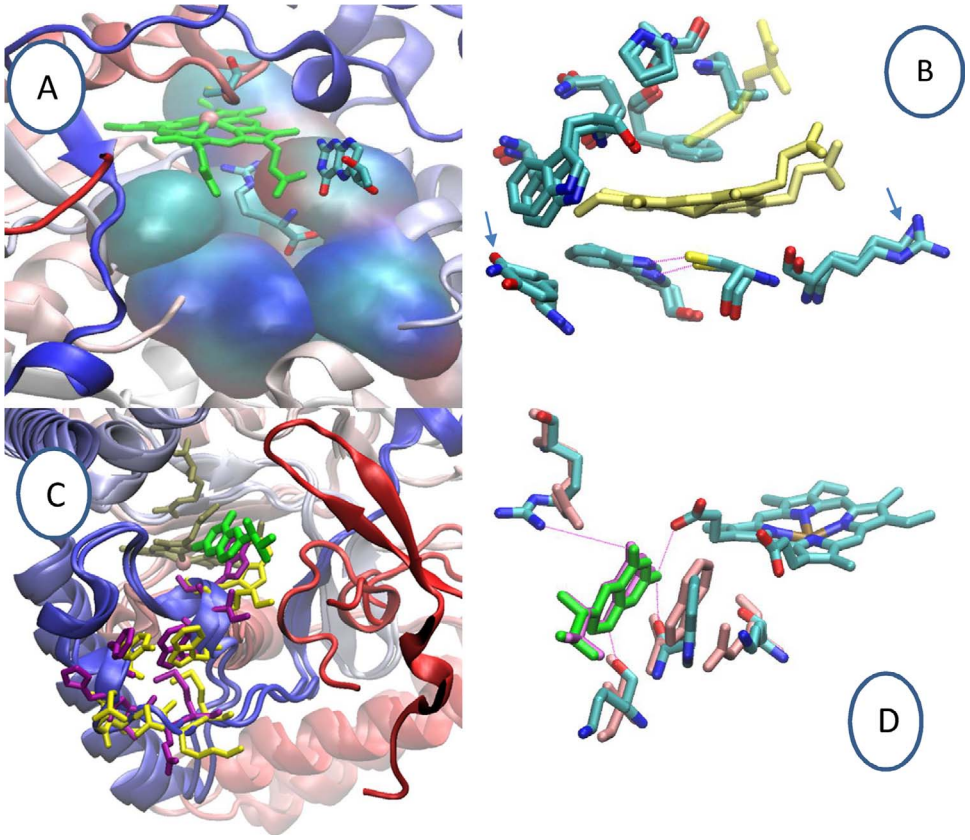

Fig. 3. Three-dimensional model of Ostreococcus tauri NOS oxygenase domain (OtNOSoxy) obtained by Homology modelling.
The model was rebuilt by modeller 9v12 using *Mus musculus* iNOSoxy crystallographic structure (1NOD) as template. Panel A. Perspective from the exposed heme edge showing the tight Arg binding pocket in OtNOSoxy structure. Residues surrounding Arg substrate are represented in quick surface mode, heme and Arg (yellow), proximal Cys and pterin (atom type color) displayed in licorice representation. Panel B. Superimposed 3D structures of the heme pocket of iNOSoxy (1NOD) and OtNOSoxy. All residues in atom-type colored licorice representation, except heme and Arg substrate that are in yellow. The mutated residues are indicated by an arrow. Panel C. Superimposed view of the heme edge and pterin binding sites of iNOSoxy (1NOD) and otNOSoxy. The two structures are superimposed in new cartoon mode representation, with N-terminal hook of iNOS in red, and C-terminal segments of both proteins in blue. Access channel residues and cofactors are represented in licorice mode: heme and Arg in tan, pterin in green, iNOSoxy residues in purple, OtNOSoxy residues in yellow. Panel D. Superimposed 3D structures of the pterin binding site highlighting the conservation of the H-bond network in both oxygenases. All residues and cofactors in licorice representation. Residues of OtNOSoxy in atom-type color mode, residues of iNOSoxy in pink. The H-bonding with pterin of three residues (K391/I456, W392/457, and R310/375), are illustrated by purple lines. Figures were generated with visualization software VMD 1.9.2.

environments. This is not the case when it comes to entry of the access channel (Fig. 3C). Some major differences are observed: i) the absence of the N-terminal hook (red β-strands), ii) a three-residues insert (406-408) that might disorder the end of the α11-helix, iii) major differences in the residues surrounding the exposed edge of the heme such as W375/Y376 (instead of H440/M441), K391 (for W456) and L420/G422 (for Y483/Y485). The modifications of the residues located at this interface, along with the opening of the channel access, might affect the dimerization process and the interaction with cofactors, among them the pterin cofactor.

3.3.3. Pterin

We thus looked at the residues of OtNOSoxy that are in interaction with the pterin. The absence of the N-terminal hook, of the N-terminal BH_4 binding region (in particular S112) and of the 3-residue insert in the helical lariat, might modify the dimer interface and affect the binding of the hydroxypropyl side chain of the pterin cofactor. However, W390 and Y405 that stands just before the insert seem to adopt the same conformation as their corresponding residues W455 and F470 in iNOS, which suggest that the helical lariat might still lock BH_4 binding pocket. The network of H-bond interaction of BH_4 with the other residues is globally conserved (Fig. 3D). However, we noticed a few modifications such as an I456-K391 conversion, a small tilt of the W392 (that might weaken the π-stacking) and the displacement of the R310 guanidinium more than 2.5 Å away from BH_4 carbonyl oxygen, strongly weakening this crucial H-bond. In general, changes in OtNOS sequence seem to lead to a looser and more open BH_4 binding pocket.

3.4. Spectroscopic characterization of native OtNOSoxy

OtNOSoxy was overexpressed and purified as described previously (see Experimental Procedures). We first recorded the UV–vis absorption spectra of OtNOSoxy in various conditions. The protein purified in the presence of Arg and BH_4 seems to fold into a functional quaternary structure characterized by a pure high spin five-coordinated (HS-5c) native complex with a Soret band maximum at 395 nm (Fig. 4A, solid line) that is identical to the ones obtained for bacterial and mammalian NOSs in the same conditions [61–63]. On the contrary, the enzyme purified in the absence of substrate and cofactor exhibits a broad Soret peak with an absorption maximum around 407 nm (Fig. 4A, dotted line), corresponding to a mixture of low spin six-coordinated (LS-6c) and HS-5c species, suggesting and uncompleted folding of OtNOSoxy into a tight dimer [46,64,65]. The presence of LS-6c species has been already reported for some bacterial (deiNOS) and mammalian (iNOS) NOSs in the absence of substrate and cofactor. The addition of saturating concentrations of Arg and BH_4 seems to induce a complete conversion of the Ls-6c species into HS-5c species, leading to a UV–vis absorption spectrum (Fig. 4A dash line) similar to the one obtained for the pure HS-5c complex. This suggests that substrate and cofactor are required to promote the folding of OtNOS into a functional conformation, alike what has been proposed for the inducible NOS [66–68].

In this conformation, OtNOSoxy is easily reduced in anaerobic conditions by addition of small amount of dithionite (Fig. 4B, dash lines; see Experimental Procedures). Addition of small amount of NO-saturated solution leads to the build-up of a ferrous heme-NO complex with an absorption maximum around 436 nm and a broad band in the α/β region, fingerprints that are characteristic of $\{FeNO\}^7$ complexes of mammalian NOSs (Fig. 4B, dotted lines). These two intermediates of NOS catalysis show the same spectroscopic fingerprint for OtNOS compared to mNOSs. This is not the case for ferrous heme-CO complex. Fig. 4C shows the UV–vis absorption spectrum of OtNOSoxy $Fe^{II}CO$ complex in the presence or absence of substrate and/or cofactor. $Fe^{II}CO$ complex were obtained by gentle CO flushing of reduced OtNOSoxy (see Experimental Procedures). In the absence of substrate and cofactor, $Fe^{II}CO$ species corresponds mostly to a 5-coordinated (5c) complex (absorption maximum around 422 nm), with a negligible fraction of 6-coordinated (6c) species (Soret at 44 nm; Fig. 4C), indicating the loss of the proximal thiolate ligand. If the addition of saturating concentrations

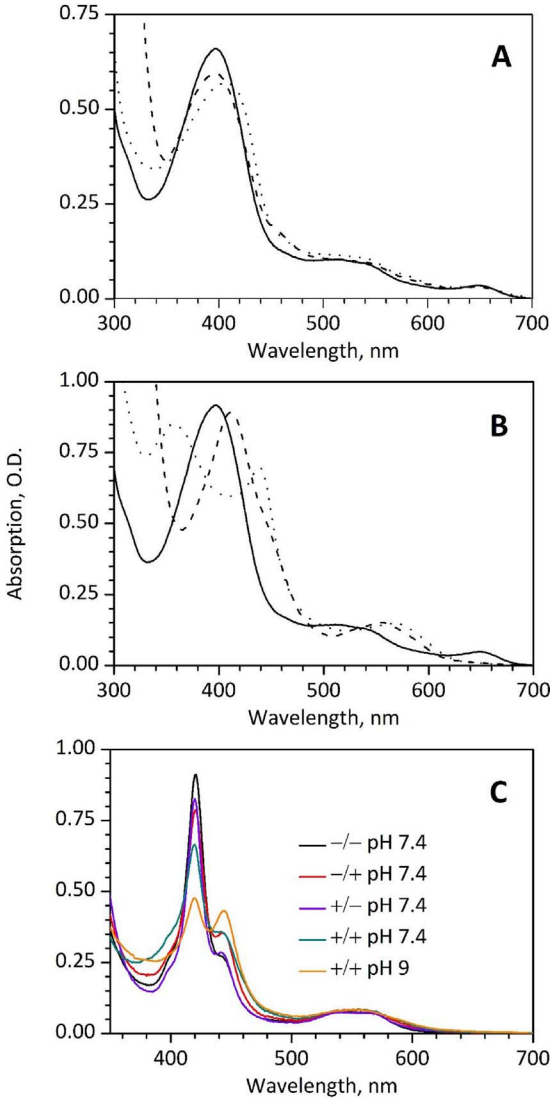

Fig. 4. Spectrophotometric characterization of major OtNOSoxy intermediates.
A) UV–visible absorption spectra of ferric OtNOS in the presence of various combinations of substrate and cofactor: purified in the absence of substrate and cofactor (dash lines), after addition of Arg and BH_4 (dotted line), purified in the presence of Arg and BH_4 (solid lines); B); Ferric heme (solid,) ferrous heme (dash) and heme-NO (dotted line) complexes of OtNOSoxy in the presence of Arg and BH_4; C) UV–visible absorption spectra of OtNOS $Fe^{II}CO$ complex under different conditions: purified at pH 7.4 in the absence of substrate and cofactor (black), after addition of Arg (red), after addition of BH_4 (mauve), in the presence of Arg and BH_4 (green) and at pH 9 (orange), in the presence of Arg and BH_4. See Experimental Procedures section.

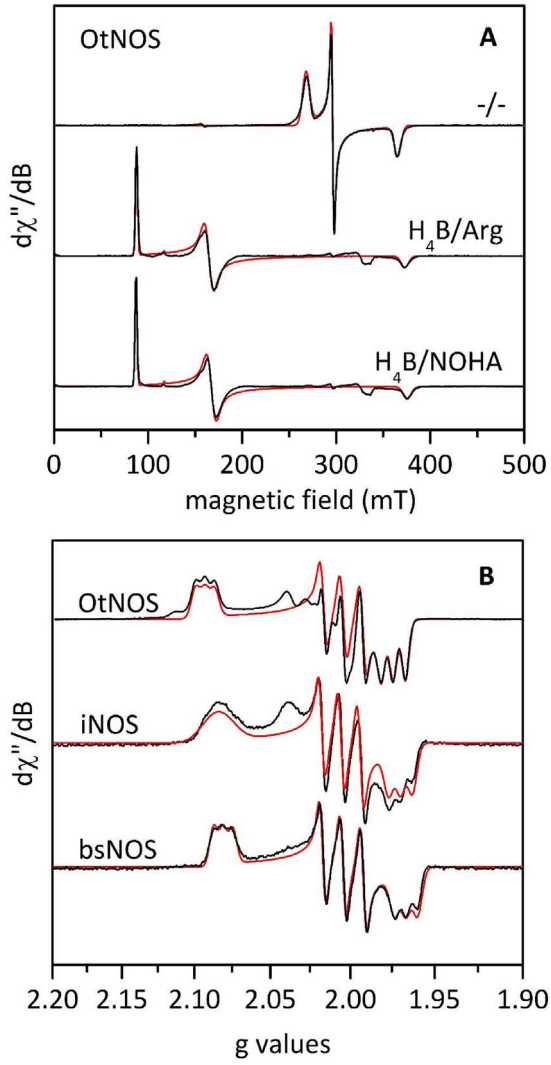

Fig. 5. Structural characterization of otNOSoxy by EPR spectroscopy.
A) Experimental (black) and simulated (red) spectra of ferric OtNOS in the presence of various combinations of substrate and cofactor. Experimental parameters: microwave frequency 9.38 GHz (Arg and NOHA) and 9.49 GHz (-/-), microwave power 1 mW (Arg), 0.25 mW (NOHA) and 0.01 mW (-/-), modulation amplitude 2 mT, temperature 10 K. B) Experimental (black) and simulated (red) spectra of otNOS $Fe^{II}NO$ complex in the presence of saturating concentrations of substrate and cofactor, spectra obtained for iNOS and bsNOS are shown for comparison. Experimental conditions: microwave frequency 9.38 GHz (OtNOS) and 9.49 GHz (iNOS and bsNOS), microwave power 0.25 μW (OtNOS) and 1 μW (iNOS and bsNOS), modulation amplitude 0.25 mT (OtNOS) and 0.4mT (iNOS and bNOS), temperature 30 K (OtNOS) and 10 K (iNOS and bsNOS).

of BH_4 does not modify the UV–vis spectrum of OtNOSoxy $Fe^{II}CO$ species, the binding of Arg slightly modifies the 5c/6c equilibrium and increases the fraction of 6c $Fe^{II}CO$ complex (Fig. 4C, violet, red and blue lines respectively). In any cases, this fraction remains minor at pH 7.4 and a significant percentage of 6c $Fe^{II}CO$ complex was to be observed only at pH 9 (Fig. 4C, orange). This suggests that the proximal ligation, essential for NOS proper catalysis [21,68], is more fragile for OtNOS complexes.

We observed the same transition by EPR spectroscopy (Fig. 5A, see experimental procedures). In the absence of substrate and cofactor, native OtNOS exhibits a LS-6c Fe^{III} EPR spectrum, well resolved, suggesting an absence of mixture between various LS-species. The simulation of the experimental spectrum (red line, see experimental procedure) leads to g values that are similar to the ones reported for iNOS water-bound LS-6c (Table 1). The addition of substrate (NOHA or Arg) and cofactor (BH_4) induces an almost complete transition towards a High-Spin species (Fig. 5A). The simulated spectra (red lines) led to the determination of the effective g values and E/D parameter (Table 1) which indicated a slightly more anisotropic system compared to iNOS with an EPR fingerprint more closely related to that of bsNOS. With respect to the nitrosyl ferrous complex of OtNOS in presence of Arg and BH_4, the EPR spectrum shows the usual rhombic pattern associated with the 6c $Fe^{II}NO$ complex as the major species. We also note as minor species the presence of the axial form at g = 2.0036 that is usually observed for the ferrous nitrosyl complexes of heme proteins [69]. The hyperfine coupling due to the NO nitrogen nucleus (^{14}N, I = 1) is particularly well resolved on all three g-values compared to other NOSs, indicating a high homogeneity of the sample and a well-defined structure of this complex. The EPR parameters obtained from the simulated spectra (Fig. 5, red lines) are reported in Table 1, they are similar to other NOSs but with increased g-anisotropy. The g-anisotropy being primarily due to spin-orbit coupling, this indicates an increased

Table 1
EPR parameters of the simulated spectra from Fig. 5.

Fe^{III} HS		g_1^{eff}		g_2^{eff}		g_3^{eff}		E/D
OtNOS	Arg/BH_4	7.65		4.07		1.80		0.077
	$NOHA/BH_4$	7.69		4.00		1.79		0.080
bsNOS	-/-	7.56		4.15		1.84		0.074
	Arg/BH_4	7.64		4.07		1.80		0.080
	$NOHA/BH_4$	7.67		3.97		1.78		0.083
iNOS	Arg/BH_4	7.54		4.12		1.82		0.075
	$NOHA/BH_4$	7.62		4.03		1.80		0.080
Fe^{III} LS		g_1		g_2		g_3		
OtNOS	-/-	2.53		2.29		1.86		
iNOS	-/-	2.42		2.29		1.91		
$Fe^{II}NO$		g_X(MHz)	A_X(MHz)	g_Y(MHz)	A_Y(MHz)	g_Z(MHz)	A_Z(MHz)	
iNOS	Arg/BH_4	2.084	30	2.005	56	1.972	34	
bsNOS	Arg/BH_4	2.081	29	2.005	59	1.967	33	
OtNOS	Arg/BH_4	2.093	29	2.004	57	1.974	34	

Abbreviations: HS high-spin, LS low-spin, g_i^{eff} effective g-values, g_i g-values, A_i hyperfine values, E/D ratio of the rhombic (E) to the axial (D) parameters of the zero-field splitting.

spin-density on the Fe ion suggesting a weakening of the bond with the proximal thiolate ligand. Indeed, we observe as well the EPR signal of a 5c complex corresponding to the loss of the thiolate proximal ligand. This observation is in agreement with the resonance Raman spectrum of the $Fe^{II}CO$ complex (see Fig. S2 in Supplementary material).

3.5. Functional characterization of OtNOSoxy

NOSs catalyze two successive steps, Arg and NOHA oxidation, that harbor different chemistry. We analyzed the ability of OtNOSoxy to catalyze Arg oxidation and release NO using stopped-flow kinetics coupled to UV–vis absorption spectroscopy in stoichiometric conditions (see Experimental Procedures). Ferrous OtNOSoxy complexes were rapid-mixed with an air-saturated buffer in the presence of BH_4 and Arg (first oxidation step) or NOHA (second oxidation step). Heme transitions were subsequently monitored and kinetics were analyzed by global analysis (see Experimental Procedures). Fig. 6A shows the superimposed spectra for the first catalytic reaction (Arg hydroxylation) recorded over the first 500 ms, highlighting the transition from ferrous (Soret band at 412 nm) to ferric OtNOS (Soret band at 398 nm and charge-transfer band around 650 nm. Kinetic traces at 650 nm depict the recovery of native HS ferric OtNOS (Fig. 6A, inset). The global analysis routine (Biologic SFIT software ©, see experimental procedures) was based on a single transition (Scheme 1, Eq. (1)) and leads to the identification of the very same complexes (ferric and ferrous heme OtNOSoxy) with similar UV–vis fingerprints. The kinetic analysis of these complexes leads to Fe^{III} build-up and Fe^{II} decay rates around $14\ s^{-1}$. These rates are similar to the ones obtained by simulating the time traces at 650 nm to a mono-exponential function ($14.1 +/- 0.3\ s^{-1}$, not shown). We achieved the same experiment for the second catalytic step in the presence of saturating concentrations of NOHA. Fig. 6B shows additional transitions with an increased absorption between 420 and 460 nm. This new band reflects the transient build-up of ferrous heme-O_2 (Soret around 428 nm and ferrous heme-NO complexes (Soret around 440 nm; See Scheme 1, Eq. (2)). Time traces show the initial decay of absorption at 395 nm (disappearance of ferrous heme) followed by ferric heme recovery after reaction completion (Fig. 6D Inset). Similarly, time traces at 442 nm show the fast build-up of a ferrous heme-NO intermediate, followed by its slow decay linked to NO dissociation. We simulated these time traces to a biexponential function corresponding to two steps: dioxygen activation and NO dissociation (Scheme 1, Eq. (2)). The simulation of the 395 nm kinetics leads to rate constants around $200 +/- 16\ s^{-1}$ (Fe^{III} decay) and $33 +/- 0.5\ s^{-1}$ (Fe^{III} recovery). Symmetrically, simulation of the 442 nm time traces leads to a $Fe^{III}NO$ build-up rate at $182 +/- 13\ s^{-1}$ and a $Fe^{III}NO$ decay rate at $45 +/- 10\ s^{-1}$. The cross-sections do not allow discriminating between $Fe^{III}NO$ and $Fe^{II}O_2$ absorption changes. The rate of the 442 nm absorption increase (and 395 nm decay) thus only reflects a global catalytic rate that includes two steps: O_2 binding and activation. However, Fe^{III} recovery at 395 nm (and 442 nm decay) is a more accurate landmark of NO dissociation rate.

We also achieved global analysis of the NOHA oxidation kinetics using SFIT protocol (see Experimental Procedure). We first try to use a 4-species model but the calculation did not converge towards significant intermediates and lead to inappropriate spectra. We repeated the analysis with a 3-species model (Scheme 1, Eq. (2)). In this case, the generated intermediate spectrum corresponded extremely well to a NOS $Fe^{III}NO$ signature (with a minor contribution of $Fe^{II}O_2$ species), confirming the catalytic production of NO. The simulation led to global catalytic rates around $82\ s^{-1}$ ($Fe^{III}NO$ build-up − oxygen activation) and $85\ s^{-1}$ ($Fe^{III}NO$ decay − NO dissociation).

Both kinetics analyses converge and led to incredibly fast rates for OtNOS catalysis. Oxygen activation rate is 5–10 times greater than the rates reported for mammalian and bacterial NOSs [18,70,71]. Even more surprising, NO dissociation seems 10–80 times faster from OtNOS than from other NOSs [22,70].

4. Discussion

4.1. Specific features of OtNOS structure

Most of the sequence alignments done so far on various NOS proteins highlight the conservation of structural elements involved in Arg binding. The whole structure that surrounds the heme-Arg moiety is present and highly conserved in OtNOS (Fig. 3B), suggesting that the key features of this structural motif has been conserved since the diverging of the algal/bacterial/metazoan NOS branches. As our phylogenetic studies place this event really early on, this indicates that this motif has been conserved through selection pressure over hundreds of millions years and is the central element of NOS biological function. Thus Arg-binding is a landmark of NOS identity and might have been involved in NOS primal biochemical activity.

However, other structural motifs are not strictly conserved. In OtNOS, many features are reminiscent of bacterial NOSs, in particular the absence of a mammalian-like N-terminal hook, including at least the first 114 residues of iNOS (up to the SIM BH_4-binding motif). This questions the nature of OtNOS quaternary structure and in particular the dimer/monomer equilibrium. Indeed the absence of the 114 first residues, or even mutations of key residues, prevents iNOS dimerization and diminishes its activity [46,55]. However, these drastic changes have been reported for bacterial NOS [19,56,72] for which it does not prevent the dimer formation. For OtNOS, the absence of a genuine Zn/S

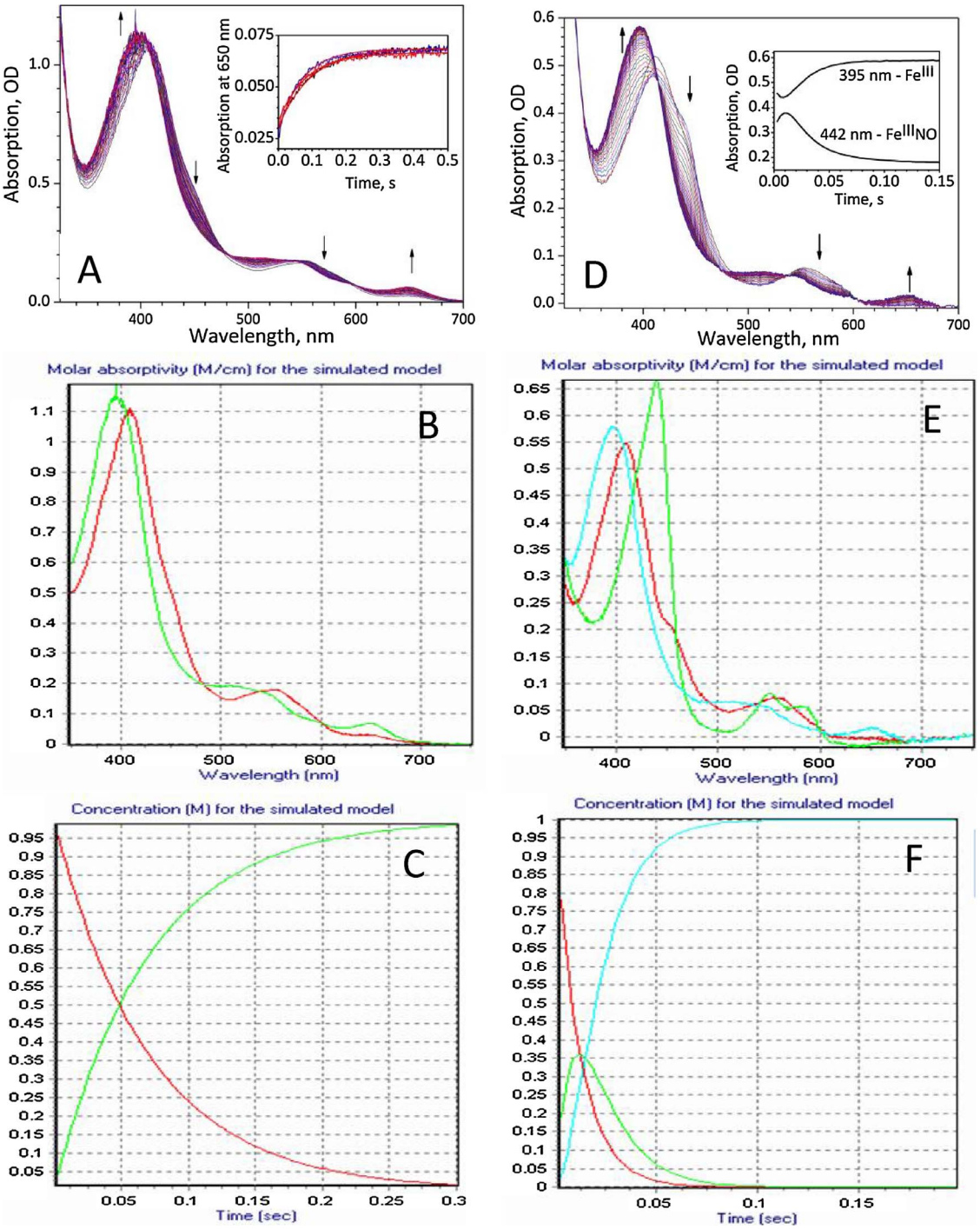

Fig. 6. Rapid-scan stopped-flow analysis OtNOSoxy catalysis.

A) Superimposed spectra of OtNOSoxy recorded for the Arg oxidation reaction. Arrows indicate the absorption increase/decrease; Inset: Time traces at 650 nm reflecting Fe^{III} heme recovery. B) Global analysis of the Arg oxidation kinetics using Sfit software with a two-intermediates model (see Experimental procedures). Sfit-calculated spectra of two distinct OtNOSoxy intermediates observed during the reaction C) Sfit-calculated kinetics of the concentration of the intermediates species; D) E) F) same as A)B)C) but for the second catalytic step (NOHA oxidation). D) Superimposed spectra of OtNOSoxy recorded for the NOHA oxidation reaction. Arrows indicate the absorption increase/decrease; Inset: Time traces at 395 and 442 nm reflecting Fe^{III} heme and $Fe^{II}NO$ absorption changes. B) Global analysis of the NOHA oxidation kinetics using Sfit software with a three-intermediates model (see Experimental procedures). Sfit-calculated spectra of three distinct OtNOSoxy intermediates observed during the reaction. C) Sfit-calculated kinetics of the concentration of these intermediates species.

cluster might not prevent the dimer conformation. The presence of a $C(X)_3C$ motif (observed for all algae NOSs but not in bacterial NOS) might instead lead to the formation of two disulfide bridges between the C45 and C49 couples, equivalent to the "swapped conformation" reported for mammalian NOS [73]. This suggests that OtNOS quaternary structure is specific of algae NOS, not related to that of mNOS but relying on additional motifs (compared to the bare bacNOS structure). Indeed, when looking at the spectroscopic fingerprints, we observe the same LS-6c/HS-5c mixture (Figs. 4 A and 5 A), suggesting the existence of an equilibrium between two conformations (monomer/dimer or loose/tight dimer).

Another aspect of OtNOS structure relates it to bacterial NOS. Alike bacterial NOS, OtNOS heme edge is more exposed, linked to changes in the N-terminal and the helical lariat regions. This questions the nature,

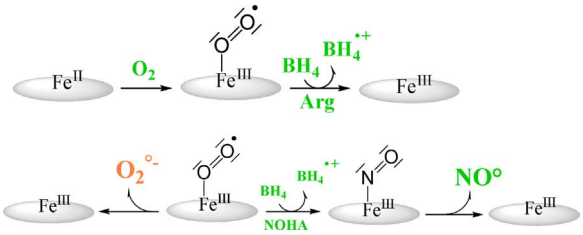

Scheme 1. The two catalytic steps of NO-Synthases.

or even binding of a pterin cofactor. Since there are no biosynthetic pathways for BH_4 in algae either, tetrahydrofolate (FH_4) could be an alternative cofactor [17,18,43]. Results obtained by Foresi et al. [43] through in vivo experiments using transgenic Arabidopsis expressing OtNOS, and in vitro assays using recombinant OtNOS, showed that OtNOS is highly active using FH_4 as cofactor. However, bacterial NOSs do not seem to harbor an optimized binding site for FH_4, apart from a few charged residues in deiNOS that could accommodate the glutamate moieties of the extended chain of FH_4 [56]. However these residues are absent in OtNOS (N389, T412, Y414) that displays a sequence closer to that of iNOS in this region. The same observation can be made for OtNOS N409 (closer to iNOS Q472 than to bsNOS R323). This region is uniquely modified in algae NOS by a small LGL insert that could also modify FH_4 binding. It appears that these motifs are not favorable to a substitution of BH_4 by FH_4, which questions the nature of the NOS cofactor (tryptophan or another heterocyclic moiety?) or even its presence.

4.2. Oxygen activation and OtNOS catalysis

Our spectroscopic investigation showed that NO ligand was binding to OtNOS ferrous heme in a standard way, with build-up of a stable 6-coordinated $Fe^{II}NO$ complex that harbors UV–vis and EPR fingerprints similar to those reported for bacNOS and mNOS. However, in the same conditions, CO binding seems to exacerbate the σ-competition, weaken the proximal thiolate (C125) ligation and leads to a predominant 5-coordinated complex (Fig. 4C). This effect is pH-dependent: at alkaline pH, the W119-C125 H-bond is more stable, decreasing thiolate electron-donating potency, which in turn leads to a weaker σ-competition and a greater 6-coordinated fraction.[2] This reflects a weaker W-S H-bond leading to a stronger "Push Effect" as we previously reported it [21].

Our kinetics investigation echoes this increased « Push Effect ». In the case of the Arg hydroxylation reaction, we observed an ultrafast $Fe^{II}O_2$ decay, illustrated by the absence of transient build-up of a $Fe^{II}O_2$. No $Fe^{II}O_2$ build-up was to be observed in the second catalytic step (NOHA oxidation) either, suggesting an ultrafast $Fe^{II}O_2$ decay, at least faster than O_2 binding. As we reported it [21,23,74], this increased decay rate is most likely related to the stronger electron donation from the thiolate, which increases both the rates of $Fe^{II}O_2$ activation or autoxidation. This does not imply that this increased Push effect is catalytically efficient, since it might lead to greater uncoupling. We indeed reported that the fine tuning of the thiolate electron-donation modulates the coupling/uncoupling balance. The question of an efficient Arg hydroxylation (and of NOHA formation) by OtNOS will depend on an appropriate synchronization of the protons transfer. In this regard, OtNOS distal heme pocket seems identical to that of mNOS and bacNOS, as can be seen from $Fe^{II}NO$ EPR fingerprint (Fig. 5B), which indicates a similar H-bond network [69,75].

In any regard, OtNOS seems to efficiently catalyze oxygen activation, without uncoupling. Indeed, kinetics analysis of the second catalytic step (NOHA oxidation) shows 100% of $Fe^{II}NO$ build-up (from global analysis report) with an ultrafast catalytic rate ($k_{cat} > 100\ s^{-1}$, beyond our set-up time resolution). This might be due to a stronger "Push Effect" or to a faster electron transfer. This rapidity might result from another molecular mechanism. Indeed, the mechanism of oxygen activation is commonly accepted for the first catalytic step (Arg Hydroxylation), but has not yet been elucidated for the second step (NOHA oxidation). If the oxygen activation by mNOS relies on the transfer of a second electron from the pterin cofactor [20,76,77], alternative mechanisms may apply for bacterial NOSs [78]. In particular, the formation of a heme-peroxide intermediate might arise from the transfer of a supplemental electron from NOHA [79–81]. In this regard, the ultrafast catalytic rate of OtNOS suggests another electron/proton transfer scheme that allows an ultrafast build-up of a heme-peroxide or oxoferryl intermediates. Moreover, OtNOS catalysis is characterized by an extraordinary fast rate of NO release for a hemoprotein. The OtNOS $Fe^{III}NO$ k_{off} rates range between 40 and 80 s^{-1} depending on the analytical procedure. This rate is at least 10–40 fold greater than the ones reported for mNOS [70] and 200 fold greater than that of bsNOS [22,82]. This ability to expulse NO might be linked to a weak geminate recombination yield [51] and a more open heme pocket, as we observed it by *in silico* homology modelling.

In brief, OtNOS seems to be a prototype for a High NO-output NOS. Along with an iNOS-related reductase domain (that favors faster electron transfer to the oxygenase), changes in the Push Effect, high k_{cat} and fast NO release could allow OtNOS to produce NO at a yet unseen rate; but for what purpose?

4.3. Origin and function of OtNOS

This question might find an answer in the phylogenetic analysis of the algae NOS family that could help understanding which NOS-related function has been conserved for many hundreds of millions of year, leading to the selection of the *OtNOS gene*. It is linked to OtNOS origin: one hypothesis is an horizontal gene transfer (HGT) event from cyanobacteria or other plankton. This should be ruled out since no cyanobacterial NOS looks like OtNOS. The 17 NOSs we identified in the cyanobacteria Phylum (spread along all sub-sections) could be classified in three different families of NOS but none of them harbors a sequence close to that of OtNOS (personal results). An HGT from a metazoan or another eukaryote is also unlikely. OtNOS gene is located on the Chromosome 17 that seems related to viridiplantae genome. Even though, a truncated OtNOS (isoform located on Chromosome 2) is believed to mostly arise from HGT).

The presence of other NOSs in other green algae phylum [42] pleads for a common ancestor to this phylum that has not been conserved in land plants. But what could have been the function required for algae NOS that would have been useless for terrestrial plants? In fact, NOSs are present in all the genomes of *Bathycoccaceae* all but that of *Ostreococcus* RCC809 (http://genome.jgi.doe.gov/). And the major difference between RCC809 and the other *Ostreoccocus* species is light exposure. *Ostreococcus* from Clades A, C, D are exposed to medium to high light and might experience photoinactivation by an oxidative stress generated in the photosynthetic chain. These organisms need to regulate Photosystem 2 activity and inhibit electron transfer chain [9]. NO might exert this activity [83] as it commonly does for the mitochondrial respiratory chain [84]. This is not the case for *Ostreococcus* RCC809 that is a deep-water organism exposed to low light intensity. RCC809 does not need a photosystem inhibitor but instead needs to maximize light photosynthesis (for example with large light harvesting collecting antenna). In a recent work, Foresi et al. [43] showed the effects of the OtNOS expression, under the control of a stress-inducible promoter, in the model plant *Arabidopsis thaliana*. Arabidopsis transgenic lines displaying a NOS-dependent (and moderate) increase of NO production, presented improved traits like fast and homogenous germination, enhanced antioxidant capacity, higher root and shoot growth, increased water content and elevated tolerance to drought

[2] In the case of NO binding, the bent conformation of the $Fe^{II}NO$ complex induces an increased π-backbonding that interferes with σ-competition.

stress. However, in order to fully address the question of the original function of otNOS and NO, two additional aspects have to be taken into account: the plurality of NO biochemical activity and the evolution of otNOS ecological niche. Because of the extremely diverse biological chemistry of NO [85], NOS activity encompasses effects as diverse as Signaling, Toxicity, Antioxidant defense, etc… Besides, there is no indication about the nature of the oxygenic environment that surrounded *Ostreoccocus tauri* (and even the Chlorophyta common ancestor), which is crucial to apprehend the nature of NOS biochemistry. In this regard, otNOS functioning and role might have radically evolved in a way that is reminiscent to the proposition made by Feelisch and Martin [86], who postulated that NO's prime role – antioxidant defense – might have been repurposed – exapted [87] – to emerging functions such as Signalling, Immunity…

By any means this topic needs more investigation at various levels such as a comparative analysis of these diverse algae, the study of functions of NOS activity in each of them through reverse genetic analyses, and the ability of algae NOS to produce other reactive oxygen and nitrogen species *in vivo*.

Appendix A. Supplementary data

Supplementary data associated with this article can be found, in the online version, at http://dx.doi.org/10.1016/j.plantsci.2017.09.019.

References

[1] W.H. Koppenol, The basic chemistry of nitrogen monoxide and peroxynitrite, Free Radic. Biol. Med. 25 (4/5) (1998) 385–391.
[2] W.C. Sessa, eNOS at a glance, J. Cell Sci. 117 (Pt 12) (2004) 2427–2429.
[3] I.N. Mungrue, D.S. Bredt, nNOS at a glance: implications for brain and brawn, J. Cell Sci. 117 (Pt 13) (2004) 2627–2629.
[4] C.J. Lowenstein, E. Padalko, iNOS (NOS2) at a glance, J. Cell Sci. 117 (Pt 14) (2004) 2865–2867.
[5] D.S. Bredt, S.H. Snyder, Nitric oxide: a physiologic messenger molecule, Annu. Rev. Biochem. 63 (1994) 175–195.
[6] J. MacMicking, Q.W. Xie, C. Nathan, Nitric oxide and macrophage function, Annu. Rev. Immunol. 15 (1997) 323–350.
[7] P. Pacher, J.S. Beckman, L. Liaudet, Nitric oxide and peroxynitrite in health and disease, Physiol. Rev. 87 (1) (2007) 315–424.
[8] A. Kumar, et al., Nitric oxide in marine photosynthetic organisms, Nitric Oxide 47 (2015) 34–39.
[9] N. Foresi, et al., Characterization of a nitric oxide synthase from the plant kingdom: NO generation from the green alga Ostreococcus tauri is light irradiance and growth phase dependent, Plant Cell 22 (11) (2010) 3816–3830.
[10] S. Messner, et al., Physarum nitric oxide synthases: genomic structures and enzymology of recombinant proteins, Biochem. J. 418 (3) (2009) 691–700.
[11] B.R. Crane, J. Sudhamsu, B.A. Patel, Bacterial nitric oxide synthases, Annu. Rev. Biochem. 79 (2010) 445–470.
[12] R. Sengupta, et al., Characterization of Drosophila nitric oxide synthase: a biochemical study, Biochem. Biophys. Res. Commun. 306 (2) (2003) 590–597.
[13] S.S. Ray, et al., Reductase domain of Drosophila melanogaster nitric-oxide synthase: redox transformations, regulation, and similarity to mammalian homologues, Biochemistry 46 (42) (2007) 11865–11873.
[14] S.S. Ray, et al., Oxygenase domain of Drosophila melanogaster nitric oxide synthase: unique kinetic parameters enable a more efficient NO release, Biochemistry 46 (42) (2007) 11857–11864.
[15] G. Werner-Felmayer, et al., Pteridine biosynthesis and nitric oxide synthase in Physarum polycephalum, Biochem. J 304 (Pt 1) (1994) 105–111.
[16] T. Agapie, et al., NO formation by a catalytically self-sufficient bacterial nitric oxide synthase from Sorangium cellulosum, Proc. Natl. Acad. Sci. U. S. A. 106 (38) (2009) 16221–16226.
[17] S.Y. Reece, J.J. Woodward, M.A. Marletta, Synthesis of nitric oxide by the NOS-like protein from deinococcus radiodurans: a direct role for tetrahydrofolate, Biochemistry 48 (23) (2009) 5483–5491.
[18] S. Adak, K.S. Aulak, D.J. Stuehr, Direct evidence for nitric oxide production by a nitric-oxide synthase-like protein from Bacillus subtilis, J. Biol. Chem. 277 (18) (2002) 16167–16171.
[19] S. Adak, et al., Cloning: expression, and characterization of a nitric oxide synthase protein from Deinococcus radiodurans, Proc. Natl. Acad. Sci. U. S. A. 99 (1) (2002) 107–112.
[20] A. Brunel, J. Santolini, P. Dorlet, Electron paramagnetic resonance characterization of tetrahydrobiopterin radical formation in bacterial nitric oxide synthase compared to mammalian nitric oxide synthase, Biophys. J. 103 (1) (2012) 109–117.
[21] A. Brunel, et al., The proximal hydrogen bond network modulates Bacillus subtilis nitric-oxide synthase electronic and structural properties, J. Biol. Chem. 286 (14) (2011) 11997–12005.
[22] Z.Q. Wang, et al., A conserved Val to Ile switch near the heme pocket of animal and bacterial nitric-oxide synthases helps determine their distinct catalytic profiles, J. Biol. Chem. 279 (18) (2004) 19018–19025.
[23] J. Lang, J. Santolini, M. Couture, The conserved Trp-Cys hydrogen bond dampens the push effect of the heme cysteinate proximal ligand during the first catalytic cycle of nitric oxide synthase, Biochemistry 50 (46) (2011) 10069–10081.
[24] F.J. Chartier, S.P. Blais, M. Couture, A weak Fe-O bond in the oxygenated complex of the nitric-oxide synthase of Staphylococcus aureus, J. Biol. Chem. 281 (15) (2006) 9953–9962.
[25] L. Lamattina, et al., Nitric oxide: the versatility of an extensive signal molecule, Annu. Rev. Plant Biol. 54 (2003) 109–136.
[26] P. Trapet, et al., NO signaling in plant immunity: a tale of messengers, Phytochemistry 112 (2015) 72–79.
[27] D. Wendehenne, et al., Free radical-mediated systemic immunity in plants, Curr. Opin. Plant Biol. 20 (2014) 127–134.
[28] M. Yu, et al., Nitric oxide function in plant biology: a redox cue in deconvolution, New Phytol. 202 (4) (2014) 1142–1156.
[29] I. Hichri, et al., Nitric oxide: a multifaceted regulator of the nitrogen-fixing symbiosis, J. Exp. Bot. 66 (10) (2015) 2877–2887.
[30] D. Wendehenne, J. Durner, D.F. Klessig, Nitric oxide: a new player in plant signalling and defence responses, Curr. Opin. Plant Biol. 7 (4) (2004) 449–455.
[31] K.J. Gupta, et al., Plant hemoglobins: important players at the crossroads between oxygen and nitric oxide, FEBS Lett. 585 (24) (2011) 3843–3849.
[32] M. Moreau, et al., NO synthesis and signaling in plants-where do we stand? Physiol. Plant. 138 (4) (2010) 372–383.
[33] M.R. Chandok, et al., The pathogen-inducible nitric oxide synthase (iNOS) in plants is a variant of the P protein of the glycine decarboxylase complex, Cell 113 (4) (2003) 469–482.
[34] F.Q. Guo, M. Okamoto, N.M. Crawford, Identification of a plant nitric oxide synthase gene involved in hormonal signaling, Science 302 (5642) (2003) 100–103.
[35] F.Q. Guo, N.M. Crawford, Arabidopsis nitric oxide synthase1 is targeted to mitochondria and protects against oxidative damage and dark-induced senescence, Plant Cell 17 (12) (2005) 3436–3450.
[36] M. Moreau, et al., AtNOS/AtNOA1 is a functional Arabidopsis thaliana cGTPase and not a nitric-oxide synthase, J. Biol. Chem. 283 (47) (2008) 32957–32967.
[37] A. Besson-Bard, A. Pugin, D. Wendehenne, New insights into nitric oxide signaling in plants, Annu. Rev. Plant Biol. 59 (2008) 21–39.
[38] T. Zemojtel, et al., Plant nitric oxide synthase: a never-ending story? Trends Plant Sci. 11 (11) (2006) 524–525 (author reply 526-8).
[39] T. Zemojtel, et al., A novel conserved family of nitric oxide synthase? Trends Biochem. Sci. 29 (5) (2004) 224–226.
[40] T. Zemojtel, R.C. Wade, T. Dandekar, In search of the prototype of nitric oxide synthase, FEBS Lett. 554 (1–2) (2003) 1–5.
[41] E. Derelle, et al., Genome analysis of the smallest free-living eukaryote Ostreococcus tauri unveils many unique features, Proc. Natl. Acad. Sci. U. S. A. 103 (31) (2006) 11647–11652.
[42] S. Jeandroz, et al., Occurrence, structure, and evolution of nitric oxide synthase-like proteins in the plant kingdom, Sci. Signal. 9 (417) (2016) re2.
[43] N. Foresi, et al., Expression of the tetrahydrofolate-dependent nitric oxide synthase from the green alga Ostreococcus tauri increases tolerance to abiotic stresses and influences stomatal development in Arabidopsis, Plant J.: Cell Mol. Biol. 82 (5) (2015) 806–821.
[44] H. Tegel, et al., Increased levels of recombinant human proteins with the Escherichia coli strain Rosetta(DE3), Protein Expr. Purif. 69 (2) (2010) 159–167.
[45] N. Foresi, et al., Analysis of the expression and activity of nitric oxide synthase from marine photosynthetic microorganisms, Methods Mol. Biol. 1424 (2016) 149–162.
[46] D.K. Ghosh, et al., Characterization of the inducible nitric oxide synthase oxygenase domain identifies a 49 amino acid segment required for subunit dimerization and tetrahydrobiopterin interaction, Biochemistry 36 (35) (1997) 10609–10619.
[47] S. Stoll, A. Schweiger, EasySpin, a comprehensive software package for spectral simulation and analysis in EPR, J. Magn. Reson. 178 (1) (2006) 42–55.
[48] B.R. Crane, et al., Structure of nitric oxide synthase oxygenase dimer with pterin and substrate, Science 279 (5359) (1998) 2121–2126.
[49] D.K. Ghosh, et al., Inducible nitric oxide synthase: role of the N-terminal beta-hairpin hook and pterin-binding segment in dimerization and tetrahydrobiopterin interaction, EMBO J. 18 (22) (1999) 6260–6270.
[50] U. Siddhanta, et al., Domain swapping in inducible nitric-oxide synthase: electron transfer occurs between flavin and heme groups located on adjacent subunits in the dimer, J. Biol. Chem. 273 (30) (1998) 18950–18958.
[51] E. Beaumont, et al., Distal Val346Ile mutation in inducible NO synthase promotes substrate-dependent NO confinement, Biochemistry 46 (47) (2007) 13533–13540.
[52] Z.Q. Wang, C.C. Wei, D.J. Stuehr, How does a valine residue that modulates heme-NO binding kinetics in inducible NO synthase regulate enzyme catalysis? J. Inorg. Biochem. 104 (3) (2010) 349–356.
[53] Z.Q. Wang, et al., Engineering nitric oxide synthase chimeras to function as NO dioxygenases, J. Inorg. Biochem. (2016).
[54] M. Weisslocker-Schaetzel, et al., Revisiting the Val/Ile mutation in mammalian and bacterial nitric oxide synthases: a spectroscopic and kinetic study, Biochemistry 56 (5) (2017) 748–756.
[55] S. Ghosh, et al., Mutational analysis of the tetrahydrobiopterin-binding site in inducible nitric-oxide synthase, J. Biol. Chem. 274 (34) (1999) 24100–24112.
[56] K. Pant, et al., Structure of a nitric oxide synthase heme protein from Bacillus subtilis, Biochemistry 41 (37) (2002) 11071–11079.
[57] B.R. Crane, et al., Structures of the N(omega)-hydroxy-L-arginine complex of inducible nitric oxide synthase oxygenase dimer with active and inactive pterins, Biochemistry 39 (16) (2000) 4608–4621.

[58] A. Sali, T.L. Blundell, Comparative protein modelling by satisfaction of spatial restraints, J. Mol. Biol. 234 (3) (1993) 779–815.
[59] B. Webb, et al., Modeling of proteins and their assemblies with the integrative modeling platform, Methods Mol. Biol. 1091 (2014) 277–295.
[60] B.R. Crane, et al., The structure of nitric oxide synthase oxygenase domain and inhibitor complexes, Science 278 (5337) (1997) 425–431.
[61] I. Rodriguez-Crespo, N.C. Gerber, P.R. Ortiz de Montellano, Endothelial nitric-oxide synthase. Expression in Escherichia coli: spectroscopic characterization, and role of tetrahydrobiopterin in dimer formation, J. Biol. Chem. 271 (19) (1996) 11462–11467.
[62] D.K. Ghosh, D.J. Stuehr, Macrophage NO synthase: characterization of isolated oxygenase and reductase domains reveals a head-to-head subunit interaction, Biochemistry 34 (3) (1995) 801–807.
[63] J. Santolini, et al., Resonance Raman study of *Bacillus subtilis* NO synthase-like protein: similarities and differences with mammalian NO synthases, Biochemistry 45 (5) (2006) 1480–1489.
[64] Y. Chen, K. Panda, D.J. Stuehr, Control of nitric oxide synthase dimer assembly by a heme-NO-dependent mechanism, Biochemistry 41 (14) (2002) 4618–4625.
[65] K. Pant, B.R. Crane, Structure of a loose dimer: an intermediate in nitric oxide synthase assembly, J. Mol. Biol. 352 (4) (2005) 932–940.
[66] W.K. Alderton, C.E. Cooper, R.G. Knowles, Nitric oxide synthases: structure, function and inhibition, Biochem. J. 357 (Pt 3) (2001) 593–615.
[67] J. Santolini, The molecular mechanism of mammalian NO-synthases: a story of electrons and protons, J. Inorg. Biochem. 105 (2) (2011) 127–141.
[68] H. Li, T.L. Poulos, Structure-function studies on nitric oxide synthases, J. Inorg. Biochem. 99 (1) (2005) 293–305.
[69] J. Santolini, et al., EPR characterisation of the ferrous nitrosyl complex formed within the oxygenase domain of NO synthase, ChemBioChem 14 (14) (2013) 1852–1857.
[70] J. Santolini, A.L. Meade, D.J. Stuehr, Differences in three kinetic parameters underpin the unique catalytic profiles of nitric-oxide synthases I: II, and III, J. Biol. Chem. 276 (52) (2001) 48887–48898.
[71] C.C. Wei, et al., The three nitric-oxide synthases differ in their kinetics of tetrahydrobiopterin radical formation: heme-dioxy reduction, and arginine hydroxylation, J. Biol. Chem. 280 (10) (2005) 8929–8935.
[72] L.E. Bird, et al., Crystal structure of SANOS: a bacterial nitric oxide synthase oxygenase protein from *Staphylococcus aureus*, Structure 10 (12) (2002) 1687–1696.
[73] B.R. Crane, et al., N-terminal domain swapping and metal ion binding in nitric oxide synthase dimerization, EMBO J. 18 (22) (1999) 6271–6281.
[74] L. Hannibal, et al., Influence of heme-thiolate in shaping the catalytic properties of a bacterial nitric-oxide synthase, J. Biol. Chem. 286 (45) (2011) 39224–39235.
[75] C.T. Migita, et al., Substrate binding-induced changes in the EPR spectra of the ferrous nitric oxide complexes of neuronal nitric oxide synthase, Biochemistry 36 (36) (1997) 10987–10992.
[76] C.C. Wei, et al., A tetrahydrobiopterin radical forms and then becomes reduced during N omega-hydroxyarginine oxidation by nitric-oxide synthase, J. Biol. Chem. 278 (47) (2003) 46668–46673.
[77] S. Stoll, et al., Nitric oxide synthase stabilizes the tetrahydrobiopterin cofactor radical by controlling its protonation state, J. Am. Chem. Soc. 132 (33) (2010) 11812–11823.
[78] Y. Zhu, R.B. Silverman, Revisiting heme mechanisms. A perspective on the mechanisms of nitric oxide synthase (NOS), Heme oxygenase (HO), and cytochrome P450s (CYP450s), Biochemistry 47 (8) (2008) 2231–2243.
[79] M.A. Marletta, A.R. Hurshman, K.M. Rusche, Catalysis by nitric oxide synthase, Curr. Opin. Chem. Biol. 2 (5) (1998) 656–663.
[80] H.G. Korth, et al., On the mechanism of the nitric oxide synthase-catalyzed conversion of N omega-hydroxyl-L-arginine to citrulline and nitric oxide, J. Biol. Chem. 269 (27) (1994) 17776–17779.
[81] K.B. Cho, J.W. Gauld, Second half-reaction of nitric oxide synthase: computational insights into the initial step and key proposed intermediate, J. Phys. Chem. B 109 (49) (2005) 23706–23714.
[82] C.A. Whited, et al., Gating NO release from nitric oxide synthase, J. Am. Chem. Soc. 134 (1) (2012) 27–30.
[83] S. Shi, et al., Protective effect of nitric oxide against oxidative stress under ultraviolet-B radiation, Nitric Oxide 13 (1) (2005) 1–9.
[84] G.C. Brown, Regulation of mitochondrial respiration by nitric oxide inhibition of cytochrome c oxidase, Biochim. Biophys. Acta 1504 (1) (2001) 46–57.
[85] D.A. Wink, K.M. Miranda, M.G. Espey, R.M. Pluta, S.J. Hewett, C. Colton, M. Vitek, M. Feelisch, M.B. Grisham, Mechanisms of the antioxidant effects of nitric oxide, Antioxid. Redox Sign. 3 (2) (2001) 203–221.
[86] M. Feelisch, J.F. Martin, The early role of nitric oxide in evolution, Trends Ecol. Evol. 10 (12) (1995) 496–499.
[87] S.J. Gould, E.S. Vrba, Exaptation – a missing term in the science of form, Paleobiology 8 (1) (1982) 4–15.
[88] M. Gouy, S. Guindon, O. Gascuel, SeaView version 4: a multiplatform graphical user interface for sequence alignment and phylogenetic tree building, Mol. Biol. Evol. 27 (2) (2010) 221–224.